

# Black-hole spectroscopy from a giant quantum vortex

Pietro Smaniotto,<sup>1,2,\*</sup> Leonardo Solidoro,<sup>1,2</sup> Patrik Švančara,<sup>1,2</sup> Sam Patrick,<sup>3</sup> Maurício Richartz,<sup>4</sup> Carlo F. Barenghi,<sup>5</sup> Ruth Gregory,<sup>3,6</sup> and Silke Weinfurter<sup>1,2,6,7,†</sup>

<sup>1</sup>*School of Mathematical Sciences, University of Nottingham, University Park, Nottingham, NG7 2RD, UK*

<sup>2</sup>*Nottingham Centre of Gravity, University of Nottingham, University Park, Nottingham NG7 2RD, UK*

<sup>3</sup>*Department of Physics, King's College London, University of London, Strand, London, WC2R 2LS, UK*

<sup>4</sup>*Centro de Matemática, Computação e Cognição, Universidade*

*Federal do ABC (UFABC), 09210-170 Santo André, São Paulo, Brazil*

<sup>5</sup>*School of Mathematics, Statistics and Physics, Newcastle University, Newcastle upon Tyne, NE1 7RU, UK*

<sup>6</sup>*Perimeter Institute, 31 Caroline Street North, Waterloo, ON, N2L 2Y5, Canada*

<sup>7</sup>*Centre for the Mathematics and Theoretical Physics of Quantum*

*Non-Equilibrium Systems, University of Nottingham, Nottingham, NG7 2RD, UK*

Black-hole spectroscopy [1] aims to infer physical properties of black holes by detecting the spectrum of quasinormal modes (QNMs) they emit while settling toward equilibrium [2–4]. Unlike normal modes, which are resonances of energy-conserving systems, QNMs are damped oscillations that arise when a system loses energy. The detection of the full spectrum is challenging due to their rapid decay, limiting observations only to the longest-lived mode [5, 6]. Theoretical [7] and numerical [8] studies suggest that environmental confinement due to surrounding plasma or dark matter can modify the QNM spectrum and enhance its detectability. Here we show that spatial confinement similarly affects the noise spectrum of nanometre-scale interface waves surrounding a giant quantum vortex in superfluid helium-4, an experimentally accessible quantum system that emulates dynamics in rotating curved spacetime [9]. In the available parameter space, we identify regimes that exhibit a multitude of QNMs whose real and imaginary frequencies are shifted with respect to those of the unbounded system, in agreement with theoretical predictions [10]. Our results highlight the versatility of quantum liquids as experimental platforms for validating theoretical toolkits in spectral stability, demonstrating their effectiveness in simulating both rotating curved spacetime and relevant environmental effects.

Recent advances in the experimental control of classical and quantum fluids [11, 12] have enabled the simulation of complex and fundamental astrophysical phenomena that are difficult to study directly. One notable example is the propagation of waves in a moving fluid, which mirrors the dynamics of a scalar field in a curved spacetime [13], providing a laboratory platform to explore the physics of rotating black holes. The rotational nature of such spacetimes gives rise to nontrivial effects, such as frame dragging [14] and the formation of an ergosphere, a region where no object can remain at rest relative to infinity. The rich phenomenology of rotating curved spacetimes thus offers a valuable framework for testing general relativity and probing potential signatures of dark matter and modified gravity theories [15]. To date, several aspects of black hole physics have been successfully reproduced in fluid systems, including Hawking radiation [16–18] and rotational superradiance [19–21]. The emission of waves related to QNMs has been studied numerically in fluids [22–25], Bose–Einstein condensates [26], exciton-polariton superfluids [27], and optical solitons [28], while experimental observations have relied on surface (gravity) waves in water [29]. These media are often dissipative, and their excitations have short lifetimes, justifying the treatment of these systems as effectively open. The absence of boundaries allows energy and information to escape to infinity.

Here, we examine the occurrence of QNMs in a newly developed gravity simulator [9] that employs surface waves (simply waves from here on) propagating on superfluid helium-4, a quantum liquid with negligible viscosity, approximately 100-times less than water [30]. Broadband fluctuations of the interface height (interface noise) are generated by minute mechanical oscillations of our experimental set-up and consist of a large number of superimposed waves. Due to the incredibly weak damping of waves in superfluid helium, the relatively small size of the system, and our ability to readout the interface noise over an extended period of time, the presence of boundaries cannot be ignored. Using a semi-analytical model [10], we have shown that spatial confinement modifies the resonance spectrum of gravitationally compact objects. The corresponding QNM frequencies shift, while their decay rates decrease, increasing the likelihood of simultaneously detecting multiple QNMs – including the longest-lived (fundamental) mode and its overtones, which experience greater damping [5]. Our experimental investigation confirms this prediction, revealing the enhanced excitation of multiple resonant modes whose frequency shifts match our model.

Our approach to explore these elusive excitations is based on a large draining vortex of superfluid helium in a cylindrical container [9]. The flow is driven by a spinning propeller acting as a centrifugal pump [31], establishing a steady recirculation loop of the superfluid between the outer glass wall and the central region, which contains a circular opening, as illustrated in Fig. 1a. The giant vortex manifests itself as a distinct, approximately

---

\* [pietro.smانيotto@nottingham.ac.uk](mailto:pietro.smانيotto@nottingham.ac.uk)

† [silke.weinfurter@nottingham.ac](mailto:silke.weinfurter@nottingham.ac)

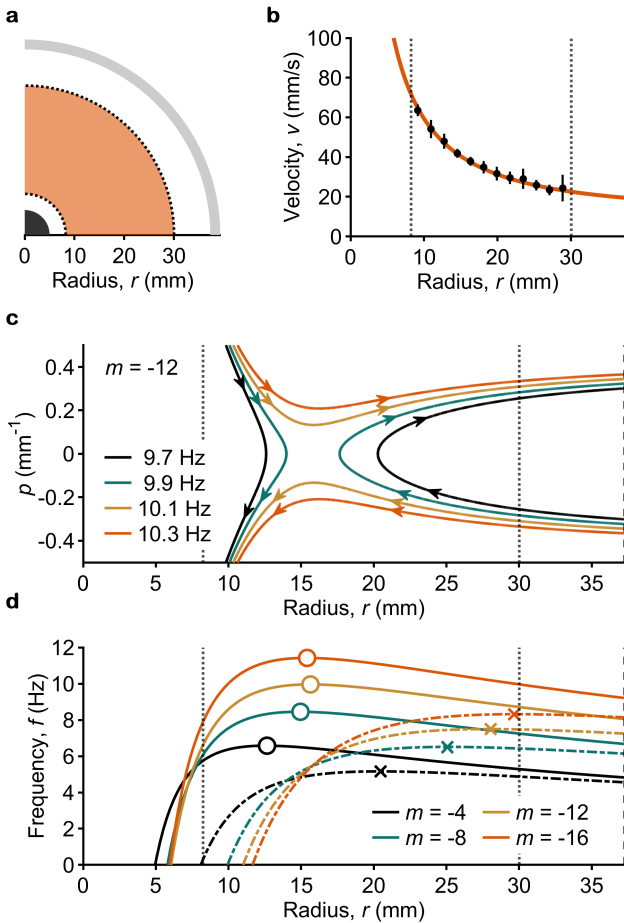


FIG. 1. **Radial phase-space trajectories and scattering potentials.** **a** Schematic top view of the experimental zone (one quadrant shown). The black region represents the drain opening (5.0 mm radius). The orange-shaded area marks the accessible field of view for interface wave detection, spanning radii from 8.2 to 30.0 mm (black dotted lines in later panels). The grey region denotes the glass wall at 37.3 mm. **b** Azimuthal velocity component of the superfluid flow as a function of radius. Black points represent values averaged over 1.8-mm radial intervals. The orange line fits Eq. (1), yielding circulation  $C = (583 \pm 3) \text{ mm}^2/\text{s}$  and a solid-body rotation frequency  $\Omega = (0.10 \pm 0.02) \text{ rad/s}$ . Vertical error bars indicate one standard deviation. **c** Phase-space diagram for the  $m = -12$  mode. The radial component of the wave vector  $\mathbf{k}$  is denoted by  $p$ . Low-frequency modes (black and green arrowed lines) reflect on both sides of the vortex-induced effective potential, while high-frequency modes (yellow and orange lines) exceeding the potential's maximum of 9.96 Hz are allowed to propagate between the giant vortex core and the outer boundary (grey dashed line). **d** Effective scattering potential, evaluated from Eq. (4) at  $p = 0$ , for four azimuthal modes (solid coloured lines). Maxima of the potential (coloured circles) correspond to light-ring frequencies. When circulation increases to  $2C$  (dash-dotted coloured lines, maxima marked by crosses), the cavity between the light ring and the outer boundary (grey dashed line) shrinks in size and depth.

15 mm deep and 5 mm wide interface depression centred above the drain. Since the vortex strength (circulation) in superfluid helium is quantum-mechanically discretised [32], the core of the giant vortex underneath the interface consists of a dense, tangled array of  $N_C = 2\pi C/\kappa = 36,600 \pm 200$  singly-quantised vortices, each carrying a circulation quantum  $\kappa = 9.98 \times 10^{-8} \text{ m}^2/\text{s}$ , yielding the circulation  $C$  of the macroscopic flow field. As  $N_C \gg 1$ , the discrete nature of the vortices can be ignored, with the giant vortex core acting as a region of continuous vorticity [32]. The rotating, curved spacetime induced by the vortex is then probed by waves that interact with its flow field. Our primary measurable is therefore the spatially and time-resolved height of the superfluid interface, which we obtain by a unique implementation of synthetic Schlieren imaging [33, 34] in a low-temperature environment. This non-invasive optical technique captures small-amplitude interface height fluctuations within an annular field of view, as illustrated in Fig. 1a.

Cylindrical symmetry and stationarity of the flow ensure the conservation of frequency  $f$  and azimuthal number  $m$ , with the latter quantifying the symmetry of a wave along a circular path. We apply a discrete Fourier transform to the time and azimuthal coordinates to decompose the height fluctuation field into individual modes labelled by  $m$  and  $f$ . Using the technique established in [9], we exploit the characteristic shape of wave spectra in Fourier space to determine the background velocity near the interface. We find that the radial velocity component is negligible in the fluid layer probed by the waves [35], while the azimuthal component exhibits a distinct radial dependence, shown by the black points in Fig. 1b. We verify that the flow field  $\mathbf{v}$ , given by

$$\mathbf{v}(r) = \left( \frac{C}{r} + \Omega r \right) \hat{\boldsymbol{\theta}}, \quad (1)$$

is almost entirely irrotational, with the contribution from the small solid-body rotation term  $\Omega r$  being subdominant with respect to the irrotational term  $C/r$ . The best fit of Eq. (1) to the experimental data is shown in Fig. 1b by an orange line.

Low-frequency waves perceive the presence of this flow field through the effective metric in one time-like and two space-like dimensions,

$$g_{ij} \propto \begin{pmatrix} -c^2 + v^2 & -\mathbf{v} \\ -\mathbf{v} & \mathbb{1}_{2 \times 2} \end{pmatrix}, \quad (2)$$

where  $c$  represents the wave propagation speed. Although this metric description does not account for the role of dispersion in influencing the dynamics of high-frequency waves, previous studies have shown that curved spacetime phenomenology persists in more general regimes [16–19, 29, 36]. To analyse the underlying wave dynamics, we employ the Wentzel–Kramers–Brillouin (WKB) approximation [37], which models interface fluctuations as a superposition of plane waves with a spatially varying wave vector

$\mathbf{k} = p \hat{\mathbf{r}} + q \hat{\boldsymbol{\theta}}$  and fixed angular frequency  $\omega = 2\pi f$ . The waves satisfy the dispersion relation [36],

$$(\omega - \mathbf{v} \cdot \mathbf{k})^2 = F(k), \quad (3)$$

where  $k \equiv \|\mathbf{k}\|$  and  $F(k)$  is the function that characterises dispersive properties of the medium (see Methods). Flow symmetries constrain the azimuthal component of the wave vector to  $q = m/r$ , but the radial component  $p$  is a free variable. Consequently, Eq. (3) admits propagating waves when  $p$  is real valued. We can find these waves as intersections of a line of constant  $\omega$  with one of the two branches of the dispersion relation,

$$\omega_D^\pm(p, m, r) = \frac{mC}{r^2} + m\Omega \pm \sqrt{F(p, m, r)}. \quad (4)$$

For the flow parameters considered here, we find at most two propagating modes at each point, corresponding to radially ingoing ( $p < 0$ ) and outgoing ( $p > 0$ ) waves. In Fig. 1c, we show how the  $p$  values of these two modes vary with radius for selected frequencies. The total wave vector defines the local wavelength,  $2\pi/k$ , which is on the order of millimetres near the outer boundary (grey dashed line) and decreases toward the centre.

We identify two distinct behaviours. At low frequency, the ingoing wave starting near the boundary is reflected by the vortex, whereas, at higher frequency, the ingoing wave propagates all the way into the centre. We understand this behaviour as follows. For  $p = 0$ , Eq. (4) exhibits a local minimum for  $\omega_D^+$  and a maximum for  $\omega_D^-$ . The frequency range between these extrema does not contain real-valued solutions, instead admitting evanescent modes characterised by imaginary  $p$ . The curve  $\omega_D^\pm(p = 0, m, r)$  then separates the propagating and evanescent solutions, acting as an effective potential barrier.

QNM arise in scenarios where the effective potential features a local maximum [3]. In our system, this occurs only for waves counter-rotating with the vortex. In Fourier space, such waves are characterised by negative azimuthal numbers and, for selected values of  $m$ , the effective potential is shown in Fig. 1d as a function of radius. The location of the maximum is analogous to the light ring in black hole physics [38, 39]. It marks the unstable boundary between waves that fall into the black-hole horizon and those that escape to infinity, as shown in Fig. 1c, and is responsible for the shape of the accretion disk in images of real black holes [40]. In our case, waves near the light ring represent the lowest-energy excitations able to radiate energy from the vortex, and approximate the real part of the fundamental QNM frequency when the WKB approximation holds.

A key factor shaping the QNM spectrum in our simulator is the presence of a boundary, which, in combination with the effective potential, forms a shallow cavity. The depth and spatial extent of this cavity are determined primarily by the circulation of the vortex. In Fig. 1d, effective potentials at double circulation values are shown

by dash-dotted lines, illustrating how the maxima shift outward and the depth of the cavity decreases. This behaviour indicates that cavity effects can only be studied within a specific range of experimental parameters, notably constraining the feasible vortex circulations. We accessed this regime through a systematic exploration of the experimental parameter space, finding effective potentials suitable for investigating confinement effects across a range of superfluid temperatures and flow drive strengths. Here, we discuss a particular realisation at temperature 1.62 K, with a driving propeller frequency of 1.67 Hz. Under these conditions, we observe numerous resonances, which are related to the QNMs of an equivalent system, featuring the same effective potential but lacking the outer boundary.

The interaction of a wave with the effective potential can be understood as a scattering process characterised by frequency-dependent reflection and transmission coefficients, respectively  $R(\omega)$  and  $T(\omega)$ , which are the ratios of the reflected and transmitted wave amplitudes to the incident wave amplitude. The purely outgoing boundary condition, indicating the absence of the outer boundary, is achieved by setting the amplitude of the incoming wave to zero, and the corresponding QNM frequencies are identified as the poles of  $R(\omega)$  and  $T(\omega)$  in the complex frequency plane. For a reflective boundary at a finite radius, the amplitudes of the ingoing and outgoing waves must satisfy an appropriate boundary condition. We found the full-slip (Neumann) boundary condition to be consistent with experimental data. Resonant modes in such a system must satisfy  $\text{Res}(\omega) = 0$ , where

$$\text{Res}(\omega) = R(\omega) \exp\left(2i \int_{r_-}^{r_B} p(r) dr\right) - 1. \quad (5)$$

The integration limits are set by the boundary position,  $r_B = 37.3$  mm, and the last scattering point,  $r_-$ , which is defined as follows. For frequencies below the light-ring frequency,  $r_-$  is the crossing point of a line of constant  $\omega$  with the effective potential. For higher frequencies,  $r_-$  corresponds to the saddle point introduced in the WKB approximation [39] (see Methods). We emphasise that modes satisfying the resonance condition are directly linked to the QNMs of the corresponding open system. As shown in [10], one can gradually increase the boundary's reflectivity and track how resonant modes shift from their original QNM frequencies to new resonances determined by evaluating Eq. (5). During this migration, the damping rate of resonant modes gets reduced, enhancing the visibility of multiple QNMs in spatially confined systems. This leads to the emergence of sharper, more distinct peaks in the frequency band just above the light-ring frequency.

Our observations of the interface noise are presented in Fig. 2 and reveal a similarly rich spectral structure. As an example, we examine azimuthal numbers  $m = -7$  and  $-12$ . Panels a and c show ensemble-averaged spectra (black lines) along with their standard deviations (grey-shaded areas). In the stationary flow studied here, steady

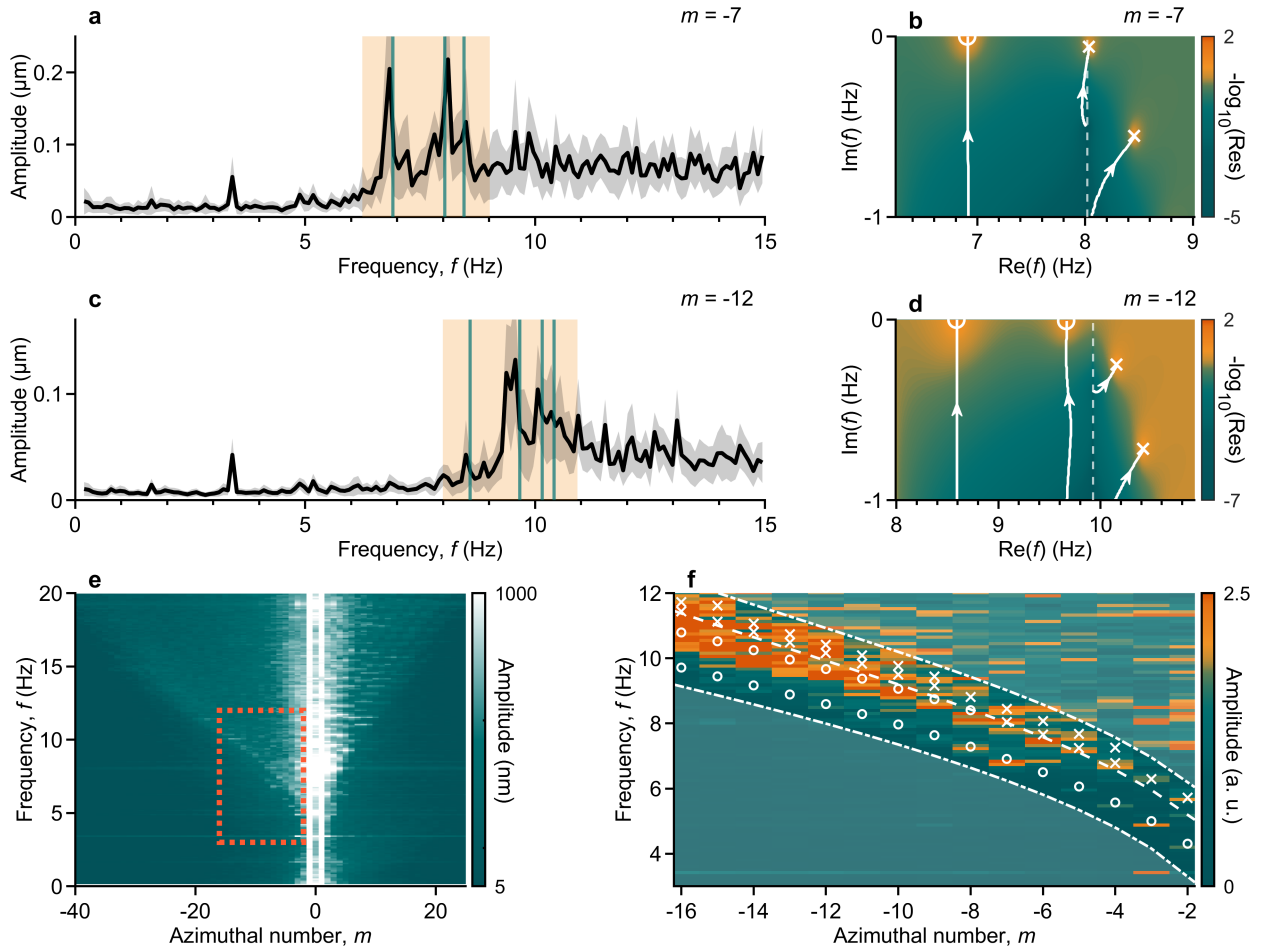


FIG. 2. **Black-hole spectroscopy.** **a, c** Ensemble-averaged spectra of surface waves (black lines) with one standard deviation intervals (grey-shaded areas) for azimuthal numbers  $m = -7$  and  $-12$ . Orange-shaded frames indicate the frequency range for the resonant mode search, delimited by the value of the effective potential at the outer boundary and the light-ring frequency incremented by 1 Hz. Green vertical lines mark the predicted resonances from panels b and d. **b, d** Maps of  $-\log_{10}(\text{Res})$  in the complex frequency plane, where Res is defined by Eq. (5). White dashed lines indicate the light-ring frequency. White symbols mark the resonances: circles for quasibound states (below the light-ring frequency) and crosses for other QNMs (above). White arrowed lines show resonance migration paths as the reflectivity of the outer boundary smoothly varies from 0 to 1. **e** Ensemble-averaged spectrogram of waves as a function of azimuthal number  $m$ . Positive (negative)  $m$  corresponds to co-rotating (counter-rotating) waves. Bound states appear for  $m > 0$ , while numerous QNMs emerge for  $m < 0$ . Bright vertical stripes at  $m = \pm 1$  are experimental artifacts. The orange dotted rectangle marks the region analysed in panel f. The colour bar follows a logarithmic scale. **f** Detailed view of the resonances from panel e. Each  $m$ -channel is ensemble-averaged and normalised by its mean amplitude. Low-frequency quasibound states (white circles) are prominent for  $m \gtrsim -10$ , while higher-frequency QNMs (white crosses) extend over a broader range of azimuthal numbers. The dashed white line marks the light-ring frequency. Dash-dotted white lines delineate the region of interest, consistent with the frequency extent in panels a and c.

excitations of specific modes enable us to average the noise spectra across overlapping time windows, reducing the contribution of random fluctuations. We perform radial averaging over a carefully selected region, excluding both the outer boundary and the giant vortex core. This approach allows us to focus on surface dynamics near the light ring (see Methods). The resulting spectra exhibit reduced amplitude at low frequencies, i.e. below the potential barrier. The first distinct amplitude peaks appear between approximately 5 and 11 Hz, around the respec-

tive light-ring frequencies, indicating the region where the least damped QNMs are predicted to be present.

In panels b and d, we evaluate Eq. (5) and plot  $-\log_{10}(\text{Res})$  in the complex frequency plane, aligning the real-axis extent with the orange-shaded regions in panels a and c. Solutions to the resonance condition,  $\text{Res}(\omega) = 0$ , appear as local maxima, marking the corresponding QNM frequencies. Modes below the light-ring frequency (white dashed line) are also known as quasibound states (white circles) and correspond to minimally-damped

waves trapped between the outer boundary and the finite potential barrier. In contrast, the damping of QNMs above the light-ring frequency (white crosses) is more significant. To illustrate how these resonances relate to the QNMs of an open system, we track their migration as the outer boundary's reflectivity smoothly varies from 0 to 1 [10]. Notably, all QNMs shift toward the real frequency axis, indicating a reduction in their decay rates. Quasibound states can be particularly identified as higher overtones of the open system that rapidly shift to lower real and nearly vanishing imaginary frequencies.

The obtained QNM frequencies are compared with the interface noise spectra in panels a and c, where they are marked by vertical green lines. The agreement between the observed and predicted excitations confirms the validity of our model and the chosen boundary condition. QNMs appear in the spectra as distinct peaks. For  $m = -7$  (panel a), peaks corresponding to the quasibound state (located at 6.9 Hz) and the fundamental QNM (8.0 Hz), are well-defined because their low damping rate corresponds to narrow peak widths. In contrast, the higher-frequency overtone (8.5 Hz) appears as a broader peak due to its faster decay. For  $m = -12$  (panel c), the experimental spectrum reveals an additional mode within the region of interest. Here, the first two quasibound states again exhibit low damping, producing narrow peaks, while other QNMs appear smeared out due to their higher dissipation rates.

Excitations above the orange-shaded regions display an additional set of peaks. These high-momentum waves only minimally interact with the effective potential and propagate between the giant vortex core and the boundary. Their dynamics are primarily influenced by interactions with the giant vortex itself. As vorticity dominates the flow inside the vortex core, accurately modelling these waves warrants further enquiries.

Panel e provides a more comprehensive view of the rich noise spectrum. It presents a full wave spectrogram, including co-rotating waves ( $m > 0$  bands). The structure in this half-plane of the Fourier space reveals bound states, which are standing waves confined between the potential barrier (for co-rotating waves, the potential diverges at small radii) and the boundary [9]. In the opposite half-plane, a broad band of excitations (brighter tones, excluding the  $m = -1$  band, which is an experimental artifact) emerges across a wide range of frequencies and azimuthal numbers. A closer examination is provided in panel f, where each azimuthal band is normalised by its mean amplitude, highlighting strong excitations matching the predicted quasibound state frequencies (white circles) and other QNM frequencies (white crosses), particularly for  $m \gtrsim -10$ . For  $m \lesssim -10$ , low-frequency modes are overshadowed by broad, higher-frequency excitations. These waves corroborate theoretical estimates of additional resonant modes (white circles and crosses), both above and below the light-ring frequency (solid white line). As higher-frequency QNMs exhibit the largest damping, their Fourier peaks acquire

a finite width, limiting the resolution of individual modes in this part of the spectrum.

Recent studies [41, 42] suggest that detecting spectral modifications in binary black hole mergers can provide valuable insights into their environments. Such observations enable detailed studies of spectral stability in black holes surrounded by plasma [43], ultralight bosonic fields [44, 45], or those in asymptotically anti-de Sitter spacetimes [46–48] where various boundary conditions have been explored. However, direct detection remains challenging, as the environmental effects may be too subtle for current or next-generation gravitational-wave detectors to resolve [41].

By confirming the predicted occurrence of multiple quasinormal modes (QNMs), our experimental platform provides compelling proof of principle, demonstrating the critical role of spatial confinement in shaping the excitation spectrum. As a next step, gravity simulators based on wave dynamics in quantum liquids will provide new opportunities to harness noise spectroscopy in bounded systems. Techniques developed for gravitational-wave analysis can be adapted to laboratory investigations, revealing additional overtones and serve as a test bed for data analysis techniques. Moreover, by refining the energy injection mechanism, whether through narrowband mechanical vibrations or controlled variations in the flow drive, we could selectively amplify specific QNMs. This process would push the system beyond the linear perturbation regime, allowing for the investigation of primary resonances scattering into an expanding family of secondary resonances [49], offering valuable insights into QNM interactions [50]. The synergy between laboratory analogues and astrophysical black holes fosters a virtuous cycle, where insights from controlled experiments feed back into our modelling of astrophysical black holes, and vice versa.

**Acknowledgements** We are grateful to Sebastian H. Völkel for valuable feedback and fruitful discussions. P.S., P.Š., S.P., C.F.B., R.G. and S.W. extend their appreciation to the Science and Technology Facilities Council for their generous support within Quantum Simulators for Fundamental Physics (ST/T006900/1, ST/T005858/1, and ST/T00584X/1), as part of the UKRI Quantum Technologies for Fundamental Physics program. L.S. and S.W. gratefully acknowledge the support of the Leverhulme Research Leadership Award (RL-2019-020). M.R. acknowledges partial support from the Conselho Nacional de Desenvolvimento Científico e Tecnológico (CNPq, Brazil, grant 315991/2023-2), and from the São Paulo Research Foundation (FAPESP, Brazil, grant 2022/08335-0). S.W. also acknowledges the Royal Society University Research Fellowship (UF120112). R.G. and S.W. acknowledge support from the Perimeter Institute. Research at Perimeter Institute is supported by the Government of Canada through the Department of Innovation, Science and Economic Development Canada and by the Province of Ontario through the Ministry of Research, Innovation and Science.

**Data & Code availability** The datasets generated and analysed during this study are available upon reasonable request. This study does not rely on custom code or algorithms beyond standard numerical evaluations.

**Materials & Correspondence** S.W. is the corresponding author. Requests for data should be addressed to P.S.

- 
- [1] K. Destounis and F. Duque, Black-hole spectroscopy: Quasinormal modes, ringdown stability and the pseudospectrum, in *Compact Objects in the Universe*, edited by E. Papantonopoulos and N. Mavromatos (Springer Nature Switzerland, Cham, 2024) p. 155–202.
- [2] K. D. Kokkotas and B. G. Schmidt, Quasi-normal modes of stars and black holes, *Living Rev. Relativ.* **2**, 2 (1999).
- [3] E. Berti, V. Cardoso, and A. O. Starinets, Quasinormal modes of black holes and black branes, *Class. Quant. Grav.* **26**, 163001 (2009).
- [4] R. A. Konoplya and A. Zhidenko, Quasinormal modes of black holes: From astrophysics to string theory, *Rev. Mod. Phys.* **83**, 793–836 (2011).
- [5] M. Giesler, M. Isi, M. A. Scheel, and S. A. Teukolsky, Black hole ringdown: The importance of overtones, *Phys. Rev. X* **9**, 041060 (2019).
- [6] C. D. Capano *et al.*, Multimode quasinormal spectrum from a perturbed black hole, *Phys. Rev. Lett.* **131**, 221402 (2023).
- [7] E. Barausse, V. Cardoso, and P. Pani, Can environmental effects spoil precision gravitational-wave astrophysics?, *Phys. Rev. D* **89**, 104059 (2014).
- [8] V. Cardoso, K. Destounis, F. Duque, R. P. Macedo, and A. Maselli, Black holes in galaxies: Environmental impact on gravitational-wave generation and propagation, *Phys. Rev. D* **105**, L061501 (2022).
- [9] P. Švančara *et al.*, Rotating curved spacetime signatures from a giant quantum vortex, *Nature* **628**, 66–70 (2024).
- [10] L. Solidoro, S. Patrick, R. Gregory, and S. Weinfurter, Quasinormal modes in semi-open systems (2024), [arXiv:2406.11013 \[gr-qc\]](https://arxiv.org/abs/2406.11013).
- [11] C. Viermann *et al.*, Quantum field simulator for dynamics in curved spacetime, *Nature* **611**, 260–264 (2022).
- [12] L. H. Dogra *et al.*, Universal equation of state for wave turbulence in a quantum gas, *Nature* **620**, 521–524 (2023).
- [13] C. Barceló, S. Liberati, and M. Visser, Analogue gravity, *Living Rev. Relativ.* **14**, 3 (2011).
- [14] B. Mashhoon, F. W. Hehl, and D. S. Theiss, On the gravitational effects of rotating masses: The thirring-lense papers, *General Relativity and Gravitation* **16**, 711–750 (1984).
- [15] E. Berti *et al.*, Testing general relativity with present and future astrophysical observations, *Class. Quantum Grav.* **32**, 243001 (2015).
- [16] S. Weinfurter, E. W. Tedford, M. C. J. Penrice, W. G. Unruh, and G. A. Lawrence, Measurement of stimulated Hawking emission in an analogue system, *Phys. Rev. Lett.* **106**, 021302 (2011).
- [17] L.-P. Euvé, F. Michel, R. Parentani, T. G. Philbin, and G. Rousseaux, Observation of noise correlated by the Hawking effect in a water tank, *Phys. Rev. Lett.* **117**, 121301 (2016).
- [18] V. I. Kolobov, K. Golubkov, J. R. Muñoz de Nova, and J. Steinhauer, Observation of stationary spontaneous Hawking radiation and the time evolution of an analogue black hole, *Nat. Phys.* **17**, 362–367 (2021).
- [19] T. Torres *et al.*, Rotational superradiant scattering in a vortex flow, *Nat. Phys.* **13**, 833–836 (2017).
- [20] M. Cromb *et al.*, Amplification of waves from a rotating body, *Nat. Phys.* **16**, 1069–1073 (2020).
- [21] M. C. Braidotti *et al.*, Measurement of Penrose superradiance in a photon superfluid, *Phys. Rev. Lett.* **128**, 013901 (2022).
- [22] V. Cardoso, J. P. S. Lemos, and S. Yoshida, Quasinormal modes and stability of the rotating acoustic black hole: Numerical analysis, *Phys. Rev. D* **70**, 124032 (2004).
- [23] E. Berti, V. Cardoso, and J. P. S. Lemos, Quasinormal modes and classical wave propagation in analogue black holes, *Phys. Rev. D* **70**, 124006 (2004).
- [24] S. Patrick, A. Coutant, M. Richartz, and S. Weinfurter, Black hole quasibound states from a draining bathtub vortex flow, *Phys. Rev. Lett.* **121**, 061101 (2018).
- [25] T. Torres, S. Patrick, M. Richartz, and S. Weinfurter, Analogue Black Hole Spectroscopy; or, how to listen to dumb holes, *Class. Quant. Grav.* **36**, 194002 (2019).
- [26] A. Geelmuyden, S. Erne, S. Patrick, C. F. Barenghi, and S. Weinfurter, Sound-ring radiation of expanding vortex clusters, *Phys. Rev. Res.* **4**, 023099 (2022).
- [27] M. J. Jacquet *et al.*, Quantum vacuum excitation of a quasinormal mode in an analog model of black hole spacetime, *Phys. Rev. Lett.* **130**, 111501 (2023).
- [28] C. Burgess, S. Patrick, T. Torres, R. Gregory, and F. König, Quasinormal modes of optical solitons, *Phys. Rev. Lett.* **132**, 053802 (2024).
- [29] T. Torres, S. Patrick, M. Richartz, and S. Weinfurter, Quasinormal mode oscillations in an analogue black hole experiment, *Phys. Rev. Lett.* **125**, 011301 (2020).
- [30] R. J. Donnelly and C. F. Barenghi, The observed properties of liquid helium at the saturated vapor pressure, *J. Phys. Chem. Ref. Data* **27**, 1217–1274 (1998).
- [31] H. Yano, K. Ohyama, K. Obara, and O. Ishikawa, Observation of the spiral flow and vortex induced by a suction pump in superfluid  $^4\text{He}$ , *J. Phys. Conf. Ser.* **969**, 012002 (2018).
- [32] C. F. Barenghi, L. Skrbek, and K. R. Sreenivasan, *Quantum Turbulence* (Cambridge University Press, 2023).
- [33] F. Moisy, M. Rabaud, and K. Salsac, A synthetic Schlieren method for the measurement of the topography of a liquid interface, *Exp. Fluids* **46**, 1021–1036 (2009).
- [34] S. Wildeman, Real-time quantitative Schlieren imaging by fast Fourier demodulation of a checkered backdrop, *Exp. Fluids* **59**, 97 (2018).
- [35] A. Andersen, T. Bohr, B. Stenum, J. J. Rasmussen, and B. Lautrup, Anatomy of a bathtub vortex, *Phys. Rev. Lett.* **91**, 104502 (2003).

- [36] S. Patrick and S. Weinfurtner, Superradiance in dispersive black hole analogues, *Phys. Rev. D* **102**, 084041 (2020).
- [37] O. Bühler, *Waves and Mean Flows* (Cambridge University Press, Cambridge, 2014).
- [38] V. Cardoso, A. S. Miranda, E. Berti, H. Witek, and V. T. Zanchin, Geodesic stability, Lyapunov exponents, and quasinormal modes, *Phys. Rev. D* **79**, 064016 (2009).
- [39] T. Torres, A. Coutant, S. Dolan, and S. Weinfurtner, Waves on a vortex: rays, rings and resonances, *J. Fluid Mech.* **857**, 291–311 (2018).
- [40] K. Akiyama *et al.* (The Event Horizon Telescope Collaboration), First M87 Event Horizon Telescope results. I. the shadow of the supermassive black hole, *Astrophys. J. Lett.* **875**, L1 (2019).
- [41] T. F. M. Spieksma, V. Cardoso, G. Carullo, M. Della Rocca, and F. Duque, Black hole spectroscopy in environments: detectability prospects (2024), [arXiv:2409.05950 \[gr-qc\]](https://arxiv.org/abs/2409.05950).
- [42] S. Roy and R. Vicente, Compact binary coalescences in dense environments can pose as in vacuum (2024), [arXiv:2410.16388 \[gr-qc\]](https://arxiv.org/abs/2410.16388).
- [43] E. Cannizzaro, A. Caputo, L. Sberna, and P. Pani, Plasma-photon interaction in curved spacetime: Formalism and quasibound states around nonspinning black holes, *Phys. Rev. D* **103**, 124018 (2021).
- [44] O. A. Hannuksela *et al.*, Probing the existence of ultralight bosons with a single gravitational-wave measurement, *Nat. Astron.* **3**, 447–451 (2019).
- [45] T. F. M. Spieksma, E. Cannizzaro, T. Ikeda, V. Cardoso, and Y. Chen, Superradiance: Axionic couplings and plasma effects, *Phys. Rev. D* **108**, 063013 (2023).
- [46] G. T. Horowitz and V. E. Hubeny, Quasinormal modes of AdS black holes and the approach to thermal equilibrium, *Phys. Rev. D* **62**, 024027 (2000).
- [47] V. Cardoso and J. P. S. Lemos, Quasinormal modes of Schwarzschild anti-de Sitter black holes: Electromagnetic and gravitational perturbations, *Phys. Rev. D* **64**, 084017 (2001).
- [48] V. Cardoso, R. Konoplya, and J. P. S. Lemos, Quasinormal frequencies of Schwarzschild black holes in anti-de Sitter space-times: A Complete study on the asymptotic behavior, *Phys. Rev. D* **68**, 044024 (2003).
- [49] S. M. D. Gregory *et al.*, Tracing the nonlinear formation of an interfacial wave spectral cascade from one to few to many (2024), [arXiv:2410.08842 \[gr-qc\]](https://arxiv.org/abs/2410.08842).
- [50] H. Yang, A. Zimmerman, and L. Lehner, Turbulent black holes, *Phys. Rev. Lett.* **114**, 081101 (2015).
- [51] S. E. Perez Bergliaffa, K. Hibberd, M. Stone, and M. Visser, Wave equation for sound in fluids with vorticity, *Physica D* **191**, 121–136 (2004).
- [52] L. A. Oliveira, C. L. Benone, and L. C. B. Crispino, Ergoregion instability in a fluid with vorticity (2024), [arXiv:2410.24161 \[gr-qc\]](https://arxiv.org/abs/2410.24161).
- [53] R. P. Feynman, Application of quantum mechanics to liquid helium, in *Progress in Low Temperature Physics*, Vol. 1, edited by C. J. Gorter (Elsevier, Amsterdam, 1957) p. 17–53.
- [54] S. Patrick, Quasinormal modes in dispersive black hole analogues (2020), [arXiv:2007.06671 \[gr-qc\]](https://arxiv.org/abs/2007.06671).
- [55] S. Iyer and C. M. Will, Black-hole normal modes: A WKB approach. I. Foundations and application of a higher-order WKB analysis of potential-barrier scattering, *Phys. Rev. D* **35**, 3621–3631 (1987).
- [56] T. Torres, Estimate of the superradiance spectrum in dispersive media, *Philos. Trans. R. Soc. A* **378**, 20190236 (2020).
- [57] E. R. Tracy, A. J. Brizard, A. S. Richardson, and A. N. Kaufman, *Ray Tracing and Beyond: Phase Space Methods in Plasma Wave Theory* (Cambridge University Press, 2014).

## METHODS

### A. Effective Hamiltonian formalism

The dispersion relation (3) describes the dynamics of waves propagating on the background of an irrotational flow,  $\mathbf{v} = \nabla\phi$ . The waves are modelled as plane-wave solutions for the fluctuations of the velocity potential  $\phi$ . Although the employed framework does not allow any vorticity degrees of freedom in these perturbations [24, 51, 52], we consider the effect of subdominant vorticity by an additional term  $m\Omega$  in Eq. (4).

Treating this term as subdominant is justified on the following grounds. The solid-body rotation term  $\Omega r$  in Eq. (1) corresponds to an array of alike-oriented single quantum vortices [53]. At the measured value of  $\Omega = 0.1$  rad/s, the mean separation between vortices is on the order of  $\delta \approx 0.1$  mm. From the perspective of a single quantum vortex, whose core has a radius  $r_c \approx 10^{-7}$  mm, the waves in our set-up can be viewed as plane waves. On the scale of one wavelength  $\lambda = 2\pi/|\mathbf{k}|$ , the vortex-induced flow field modifies the wavefront by a phase shift

$$\Delta\Phi \approx N \frac{|\mathbf{k}| r_c c_s}{v_g}, \quad (6)$$

where  $N$  is the number of free vortices,  $c_s$  is the speed of sound in superfluid helium and  $v_g$  is the group velocity. We estimate  $N = (\lambda/\delta)^2 \approx 10^2$ . Since  $c_s/v_g \approx 10^3$  and  $r_c/\lambda \approx 10^{-7}$ , we find  $\Delta\Phi \approx 10^{-2}$  rad, indicating that the plane wave remains largely unaltered by these few vortices and their collective effect can be treated as subdominant compared to the irrotational flow induced by the giant quantum vortex in the centre of the experimental zone.

In Eq. (4),  $F$  denotes the dispersion function, which reads for gravity-capillary waves,

$$F(k) = (g + \gamma k^2)k \tanh(h_0 k), \quad (7)$$

where  $k \equiv |\mathbf{k}|$ ,  $g$  is the gravitational acceleration,  $\gamma = 2.25 \times 10^{-6}$  m<sup>3</sup>/s<sup>2</sup> is the ratio of surface tension and density at 1.62 K [30] and  $h_0 = 28$  mm is the equilibrium interface height.

Waves propagate in the laboratory frame with group velocity  $\nabla_k \omega = \mathbf{v} \pm \nabla_k \sqrt{F(k)}$ . Since the group velocity varies with  $k$ , the waves are, in general, dispersive. Light rings can be defined in dispersive systems by introducing an effective Hamiltonian [36, 39, 54],

$$\mathcal{H} = -\frac{1}{2}(\omega - \omega_D^+)(\omega - \omega_D^-), \quad (8)$$

where  $\omega_D^\pm$  denotes the two branches of the dispersion relation given by Eq. (4). The condition

$$\mathcal{H} = 0 \quad (9)$$

enforces the dispersion relation (3) while the wave dynamics is given by Hamilton's equations,

$$\dot{r} = \partial_p \mathcal{H}, \quad \text{and} \quad \dot{p} = -\partial_r \mathcal{H}. \quad (10)$$

A mode trapped in the light ring follows an unstable circular trajectory, satisfying the dispersion relation together with the following conditions,

$$\partial_p \mathcal{H} = 0, \quad \text{and} \quad \partial_r \mathcal{H} = 0. \quad (11)$$

The points that satisfy Eq. (11) are the saddle points of the dispersion function, generalising the notion of the potential's maximum which scatters frequencies around the light-ring [23] to the dispersive regime. In fact, for fixed frequency  $\omega$  and azimuthal number  $m$ , the first condition in Eq. (11) returns  $p = 0$ , while the second gives the radius of the circular orbit,  $r_{\text{sp}}$ . It follows that saddle points lying on the positive branch of the dispersion relation  $\omega_D^+(r, p)$ , i.e. obeying Eq. (9), satisfy

$$\partial_p \omega_D^+ = 0, \quad \text{and} \quad \partial_r \omega_D^+ = 0, \quad (12)$$

which correspond to the local maxima highlighted in Fig. 1d by open circles.

The WKB approximation breaks down near the saddle points because of the divergence of the corresponding wave amplitudes. A well-known matching procedure [29, 39, 54] solves this issue by introducing a transfer matrix that relates the mode amplitudes on both sides of  $r_{\text{sp}}$ . Keeping  $\omega$  and  $m$  fixed, the radial part of the wave in the proximity of the saddle point takes the form,

$$\begin{aligned} \phi(r) \propto & \alpha^+(r_{\text{sp}}) \exp\left(i \int_{r_{\text{sp}}}^r p(r') dr'\right) + \\ & + \alpha^-(r_{\text{sp}}) \exp\left(-i \int_{r_{\text{sp}}}^r p(r') dr'\right), \end{aligned} \quad (13)$$

where  $\alpha^\pm$  denote the complex amplitudes of radially in-going and outgoing modes. The transfer matrix relates amplitudes on both sides of the saddle point  $r_{\text{sp}}^\pm$  [55–57],

$$\begin{bmatrix} \alpha^+(r_{\text{sp}}^-) \\ \alpha^-(r_{\text{sp}}^-) \end{bmatrix} = -ie^{-\pi\varrho} \begin{pmatrix} 1/\bar{R} & -1 \\ 1 & 1/\bar{R}^* \end{pmatrix} \begin{bmatrix} \alpha^+(r_{\text{sp}}^+) \\ \alpha^-(r_{\text{sp}}^+) \end{bmatrix}, \quad (14)$$

where the coefficient  $\bar{R}$  is given by

$$\bar{R} = -i \frac{(\sqrt{\varrho})^{2i\varrho} e^{-\varrho(i+3\pi/2)}}{\sqrt{2\pi}} \Gamma(1/2 - i\varrho), \quad (15)$$

with

$$\varrho = -\frac{\mathcal{H} \text{sign}(\partial_p^2 \mathcal{H})}{\sqrt{-\det(d^2 \mathcal{H})}}. \quad (16)$$

The term  $d^2 \mathcal{H}$  in the denominator of the relation above denotes the Hessian of  $\mathcal{H}$  and all quantities are evaluated at  $p = 0$  and  $r = r_{\text{sp}}$ .

In order to determine resonant modes, we impose a purely absorptive boundary condition in the origin by requiring  $\alpha^+(r_{\text{sp}}^-) = 0$ . Then, the local reflection coefficient  $R(\omega) = \alpha^+(r_{\text{sp}}^+)/\alpha^-(r_{\text{sp}}^+)$  used in Eq. (5) is given by Eq. (15). The Neumann boundary condition at  $r = r_B$  is



implemented by requiring  $\alpha^+(r_B) = \alpha^-(r_B)$ . Note that here we are neglecting the effects of the meniscus and fluid flow at the boundary, which require further investigation. Finally, one obtains the resonance condition (5) by relating the wave amplitude near the saddle point and the boundary.

The resonance condition is evaluated in the complex frequency plane for  $m = -7$  and  $-12$  in panels b and d in Fig. 2. The agreement between experimental data and numerical predictions confirms the validity of our model, which assumes an irrotational, inviscid flow with an absorbing core.

### B. Stationary QNMs

QNMs in open systems radiate energy from their source to infinity. These modes are therefore inherently decaying and their amplitudes eventually vanish once the available energy is depleted. In the present case, the stationary vortex flow is established through an external drive [9]. Mechanical vibrations of the glass wall confining the set-up (see Fig. 1a) constantly excite waves over a broad frequency range, facilitating the observation of excitations both co- and counter-rotating with the superfluid (see Fig. 2e).

Resonant modes studied here are observed in the stationary regime. That is, we record the superfluid interface 60 s after the vortex flow is established, for a duration of 20.5 s (4096 frames at a rate of 200 frames per second). During the acquisition window, we did not observe any qualitative changes in the dynamics of the interface. We demonstrate this in Fig. 3, where we display time-dependent spectrograms for  $m = -7$  (panel a) and  $-12$  (panel c). Dominant excitations correspond to

the predicted frequencies, marked A-C and A-D, respectively, and their amplitudes are shown in panels b and d as a function of time. Therein, we only observe submicrometre, unstructured amplitude fluctuations. Due to their stationarity, we study these excitations by means of the ensemble-averaged frequency spectra. As specified in the main text, the averaging is performed in the radial direction between 12.4 and 27.8 mm, and in overlapping time windows of 10.2 s duration.

In addition, we note that the high-momentum-amplitude peaks shown in Fig. 2f appear to be broadened. This can be explained in part by the damped nature of QNMs (damping being proportional to the imaginary part of their frequency), but also by external mechanical noise. The broadening is equally visible in Fig. 2c for the highest frequency resonances, which are the most damped (cf. Fig. 2d). An additional source of frequency variation is due to the continuous evaporation of the superfluid. For similar experimental conditions as those considered here (1.62 K), we estimate the evaporation rate (rate of change of interface height) to be  $10 \mu\text{m/s}$ , resulting in the change of the interface height of approx. 0.2 mm during one data acquisition run. This effect modifies the effective potential and induces small frequency shifts to resonant modes, while the evaporation only minimally affects the interface detection method employed, introducing errors smaller than 1%.

We have shown that the system can be considered stationary, with amplitude fluctuations arising from unstructured submicrometre waves, and the broadening of spectral peaks resulting from the inherent damping of QNMs, mechanical noise, and possibly from the continuous loss of superfluid helium in the experiment. The combined impact of these effects on our measurements of the height fluctuation field is, nonetheless, marginal.

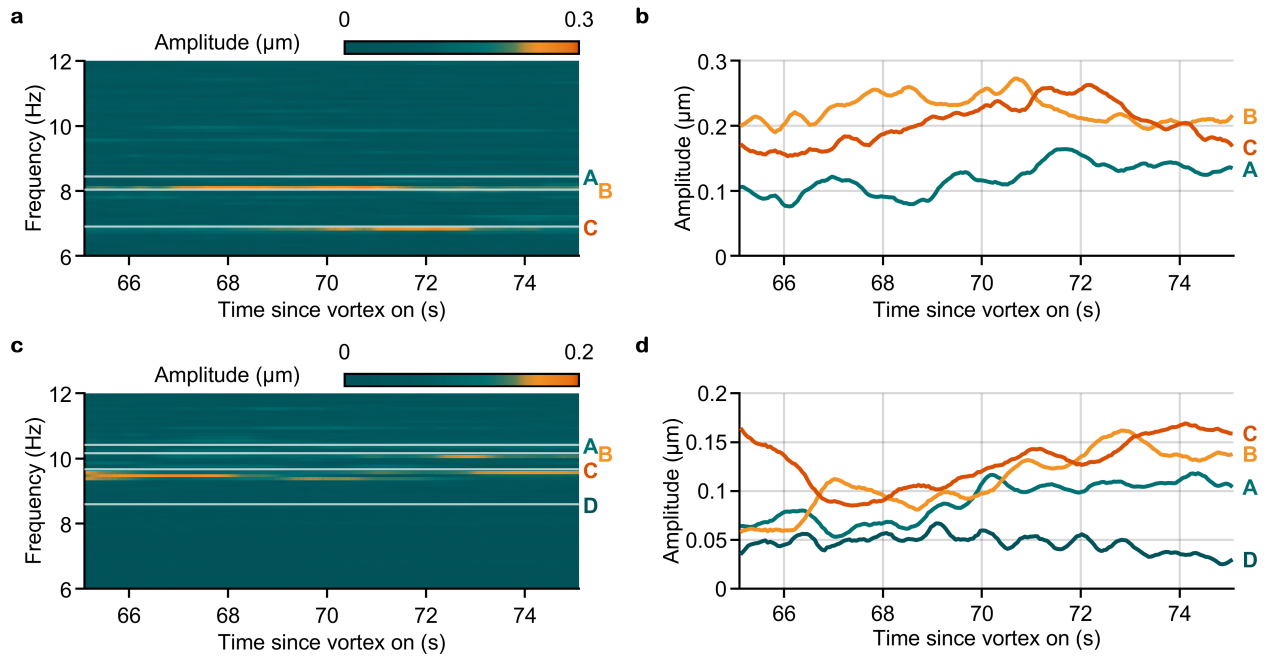


FIG. 3. **Time invariance of QNMs.** **a,c** Spectrogram of waves, plotted as a function of time for selected azimuthal modes  $m = -7$  (top panels) and  $-12$  (bottom panels). White horizontal lines mark predicted resonances and are labelled A-D with descending frequency order. **b,d** Amplitudes of the extracted excitations (labelled according to panels a, c) as a function of time. The amplitudes undergo sub-micrometre variations, therefore they are to be considered stationary compared to the evaporation rate of the superfluid and the overall ambient noise.